Ca₄Nb₂O₉–CaTiO₃: Phase Equilibria and Microstructures

L. A. Bendersky, I. Levin, R. S. Roth, and A. J. Shapiro

Materials Science and Engineering Laboratory, NIST, 100 Bureau Drive, Stop 8554, Gaithersburg, Maryland, 20899-8554

$CaTiO_3$–$Ca_4Nb_2O_9$ is a quasi-binary section, and all the phases participating in equilibrium are solid solutions of the binary end-members. The phases are perovskite-based ABO_3-type, with a common stoichiometry $Ca[Ca_xNb_yTi_z]O_3$. The differences between the lower-temperature phases is in the type of ordering between Ca/Nb/Ti ions occupying the *B*-site, as well as in the type of octahedral tilting. The proposed phase diagram has the following single-phase fields: (1) cubic disordered C (*Pm$\bar{3}$m*); (2) a series of disordered/tilted $CaTiO_3$-based polymorphs T, O_1, and O_2 (*Pnma*) with different combinations of tilting; (3) disordered/tilted O_2' (*Pnma*), same as O_2 but lower in Ti; (4) ordered/tilted HTP_2 (*P2$_1$/c*) with 1:1 ordered $(111)_c$ planes; (5) ordered/tilted $LT_{1/6}$ (*P2$_1$/c*) with 1:2 ordered $(111)_c$ planes. The single-phase fields are connected with the following reactions of the phases: (1) high-temperature monotectoid $C \rightarrow C' + O_2'$; (2) miscibility gap $C \rightarrow C' + C''$; (3) eutectoid $HTP_2 \rightarrow LT_{1/6} + O_2$; (4) a series of peritectoid reactions between O_2' and $CaTiO_3$ polymorphs; (5) an ordering transition $O_2' \rightarrow HTP_2$. In addition, a metastable transition to the triclinic $LT_{1/4}$ phase (with 1:3 ordered $(111)_c$ planes) occurs for a wide range of compositions $(0 < x < 0.6)$.

Key Words: $CaTiO_3$–$Ca_4Nb_2O_9$; phase diagram; phase transformation; TEM; dielectrics.

1. INTRODUCTION

Perovskite is an important structural base for many materials with important physical properties, such as dielectric, ferroelectric, magneto-resistive, etc. Some of the best dielectric materials used in microwave communication devices are complex $(A,A')(B,B')O_3$ oxides with perovskite-like structures. Such oxides have been intensively studied with the goal of understanding the interrelationships between dielectric properties and crystallo-chemical characteristics (type of *A*-site and *B*-site ions, distortions of BO_6 octahedra, chemical ordering between either $A–A'$ or $B–B'$ ions, domain substructure) (1). Recently, promising dielectric properties of perovskite-based $Ca_5Nb_2TiO_{12}$ (or $4Ca(CaNb_2Ti)_{1/4}O_3$) were reported (2). In this study a systematic dependence of the dielectric constant *K* and its temperature coefficient d*K*/d*T* on processing conditions

was found. These effects were attributed to an order-disorder transition on the *B*-site; however, no direct evidence for such a transition was presented.

The possible chemical ordering in $Ca_5Nb_2TiO_{12}$ can be related to the *B*-site ordering observed in the binary $Ca_4Nb_2O_9$ compound (pseudo-perovskite $3Ca(CaNb_2)_{1/3}O_3$) (3, 4). Combining the interest in better understanding the $Ca_5Nb_2TiO_{12}$ composition with possible improvement of properties by incorporating more of the very high dielectric constant $CaTiO_3$ perovskite, the study of $xCaTiO_3$–$(1-x)Ca_4Nb_2O_9$ quasi-binary section of the ternary $CaO–TiO_2–Nb_2O_5$ phase diagram appears to be important. To the best of our knowledge, no other reports on the phase equilibria in $CaTiO_3$–$Ca_4Nb_2O_9$ have been published. Since both end-members have perovskite-based structures, it is expected that the complete quasi-binary section can be considered as $Ca[Ca_{(1-x)/(3-2x)}Nb_{(2-2x)/(3-2x)}Ti_{x/(3-2x)}]O_3$, with the *A*-sites occupied by Ca, and the *B*-sites by Ca, Ti, and Nb. Based on the aforementioned studies of $CaTiO_3$ and $Ca_4Nb_2O_9$, the $CaTiO_3$–$Ca_4Nb_2O_9$ section is expected to have a high-temperature ideal (cubic) perovskite solid solution and low-temperature perovskite-based phases, which are similar (or related) to the structure of the end-members. Because of the structural relationship between the phases, we anticipate microstructures based on either coherent or semicoherent phase equilibria between phases residing on a common lattice of the cubic perovskite. For such a system the understanding of crystallographic details is imperative, and hence, the use of transmission electron microscopy (TEM) is very appropriate.

2. STRUCTURES OF THE END-MEMBERS

2.1. CaTiO₃

$CaTiO_3$ (the mineral *perovskite*) exists in several polymorphic forms which differ by a distortion of the framework of corner-connected $[TiO_6]$ octahedra. The distortion originates from a large mismatch in the size of the *A*-type (Ca^{2+}) and *B*-type (Ti^{4+}) cations (tolerance factor $t = (R_A + R_O)/2(R_A + R_B) = 0.8768$) and can be approximated

by a set of rotations (tilts) of rigid $[BO_6]$ octahedra (5). A recent structural refinement of the high-temperature powder neutron diffraction data suggested a sequence of space groups and types of distortion (in the form of a combination of tilts according to Glazer's notations) (6). The results are summarized in Table 1. Earlier studies (7–9) suggested somewhat different transition temperatures and the sequence of tilts, as well as the space group of the intermediate tetragonal phase. Nevertheless, the structure of the low-temperature phase ($< 1100°C$) is well established as orthorhombic with space group *Pnma*, #62. In the coordinates of the *Pnma* space group, the octahedra are tilted around the four-fold *b*-axis (b^+ in-phase tilt) and around the two-fold *a*-axis (a combination of two antiphase tilts $a^- a^-$). A schematic drawing of the tilted *Pnma* $CaTiO_3$ structure is shown in Fig. 1. Figure 2 shows schematic drawings of $\langle 110 \rangle$-type selected area electron diffraction (SAED) patterns for a variety of phases discussed in the paper (indexing without a subscript in this paper indicates a cubic lattice). These schematics will be used in the further analysis of TEM diffraction patterns. Figure 2a is a SAED pattern of the undistorted cubic perovskite (a_p). Figure 2b shows two nonequivalent $\langle 110 \rangle$ patterns of the *Pnma* structure. The pattern indexed as $[001]_O$ (O, orthorhombic $\sqrt{2}a_p \times 2a_p \times \sqrt{2}a_p$ lattice) has a zone axis normal to both b^+ and combined $a^- a^-$ tilting axes.

$Ca_4Nb_2O_9$

Three ordered perovskite-based polymorphs exist for the $Ca_4Nb_2O_9$ compound, Table 2 (3, 4). The polymorphs were determined by Levin *et al.* (4) as structures combining a tilt of octahedra (tolerance factor $t = 0.82$) and ordering of Ca,Nb on a mixed *B*-site. The tilt system for all three polymorphs is the same as for the low-temperature polymorph of $CaTiO_3$: $a^- b^+ a^-$. The Ca,Nb ordering for all three polymorphs occurs between differently occupied (111) planes and, therefore, is characterized by an ordering *k*-vector along $[111]^*$. Three polymorphs were found to
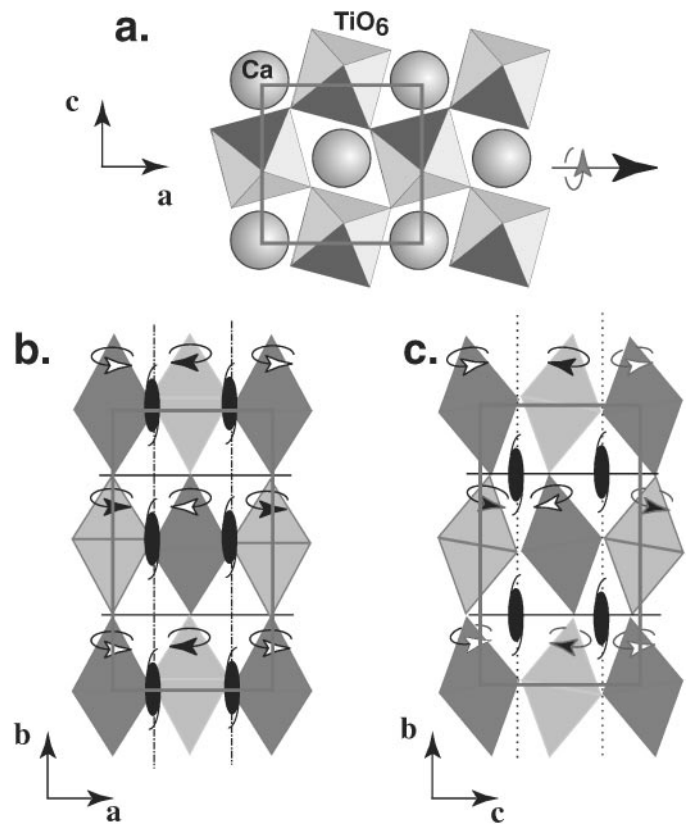

FIG. 1. A schematic drawing showing three main projections, (a) $[010]_O$, (b) $[001]_O$, and (c) $[100]_O$, of the orthorhombic *Pnma* structure of $CaTiO_3$. In (a) both the *A*-site Ca ions and TiO_6 octahedra are shown. In (b) and (c) only TiO_6 octahedra, as well as selected symmetry elements of the *Pnma* space group, are shown for simplicity. Different shadows of the octahedra represent different planes of their location.

exhibit the following ordering of the (111) *B*-cation planes:

(1) 1:1 ordering for the pseudo-cubic, monoclinic HTP_2 phase with $P2_1/c$ space group [known in mineralogy as *elpasolites* (10,11)] and lattice parameters $\approx \sqrt{2}a_p \times \sqrt{2}a_p \times \sqrt{6}a_p$, $\beta \approx 125°$;

TABLE 1
Polymorphs of $CaTiO_3$

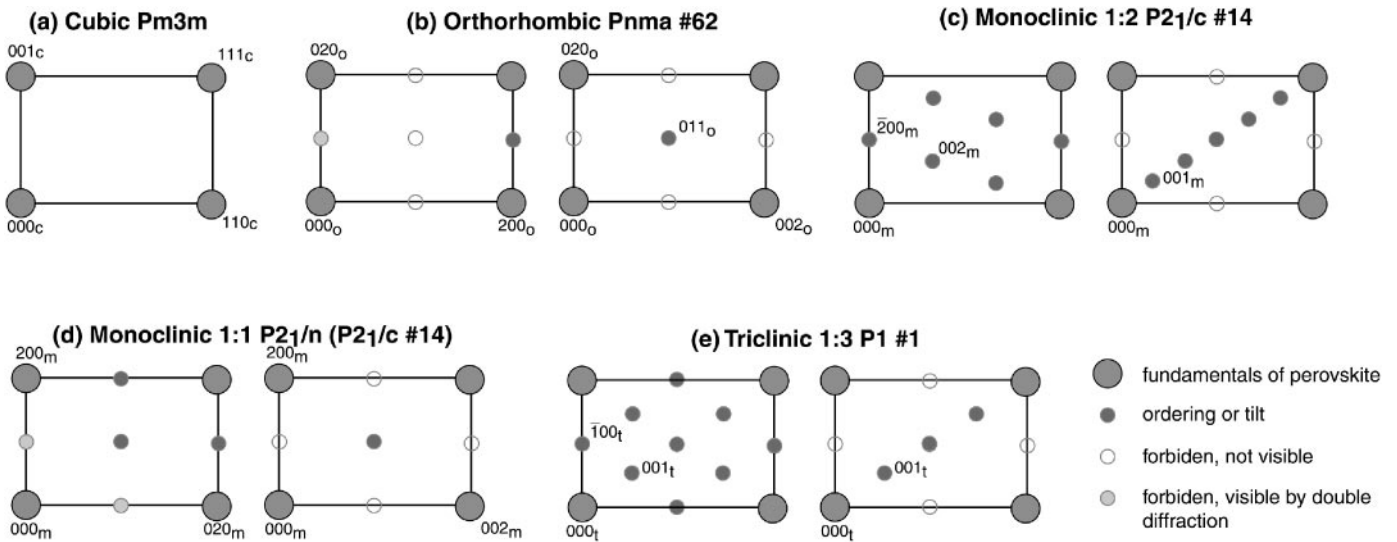| Polymorphs	Temperature of existence	Space group, #	Ordering **k** vector	Distortion/tilt
Cubic (C)	$> 1307°C$ (> 1247)[a]	*Pm3m*, #221	None	None
Tetragonal (T)	$1227°C$–$1307°C$	*I4/mcm*, #140 (*P4/mbm*, #127)	$\frac{1}{2}[110]^*$	$a^0 a^0 c^-$ ($a^0 a^0 c^+$)
Orthorhombic (O_1)	$1107°C$–$1227°C$ ($1111°C$–?)	*Cmcm*, #63	$\frac{1}{2}[111]^*$	$a^0 b^+ c^-$
Orthorhombic (O_2)	$< 1107°C$ ($< 1111°C$)	*Pnma*, #62	$\frac{1}{2}[111]^*$	$a^- b^+ a^-$

[a]In parentheses results from (7, 8).

FIG. 2. A schematic drawing of the $\langle 110 \rangle$-type SAED patterns for different perovskite-related structures of Ca$_4$Nb$_2$O$_9$ polymorphs. The patterns are indexed according to the space groups proposed in Ref. (4).

(2) 2:1 ordering for the monoclinic LT$_{1/6}$ with $P2_1/c$ space group and lattice parameters $\approx \sqrt{6}a_p \times \sqrt{2}a_p \times 3\sqrt{2}a_p$, $\beta \approx 125.5°$;

(3) 3:1 ordering for the triclinic LT$_{1/4}$ with apparent $P1$ space group and lattice parameters $\approx \sqrt{6}a_p \times \sqrt{2}a_p \times 2\sqrt{2}a_p$, $\alpha = \gamma \approx 90°$, $\beta \approx 125.5°$.

The different ordered polymorphs can be distinguished by the positions of the superlattice reflections in the $\langle 110 \rangle$-type SAED patterns, Fig. 2. In this drawing, the pairs of nonequivalent $\langle 110 \rangle$-type SAED patterns are presented, with all left-side patterns corresponding to the orientation of octahedral tilting shown in Fig. 1b. The drawing demonstrates that all phases can be distinguished from each other by the SAED patterns.

3. EXPERIMENTAL METHODS

The xCaTiO$_3$–(1–x)Ca$_4$Nb$_2$O$_9$ specimens were synthesized by solid-state reaction in air using high-purity CaCO$_3$, Nb$_2$O$_5$, and TiO$_2$. Specimens were initially prepared at NIST every 10 mo/% and then, as more data were found to be needed, at every 5 mo/% from Ca$_4$Nb$_2$O$_9$ to 50% CaTiO$_3$. X-ray powder diffraction patterns of these specimens, both annealed at and quenched from the temperatures shown in Fig. 3, were analyzed. The quenched specimens were reheated at lower temperatures to determine reversibility of the phase reactions. The resultant diagram, Fig. 3, although representative of the X-ray data obtained at room temperature, was not satisfactory to explain all of the results of the dielectric data (2). Therefore, several compositions were selected and prepared for examination by TEM, which constituted the main study of the paper. In addition, the specimens with $x = 0.5$ used for the dielectric measurements in (2) were kindly provided by Prof. R. Cava of Princeton University. For the compositions prepared at NIST the following procedure was used. Before each heating a mixture was ground for 20 min using an agate mortar and pestle; the initial grinding was carried out in ethanol

TABLE 2
Polymorphs of Ca$_4$Nb$_2$O$_9$

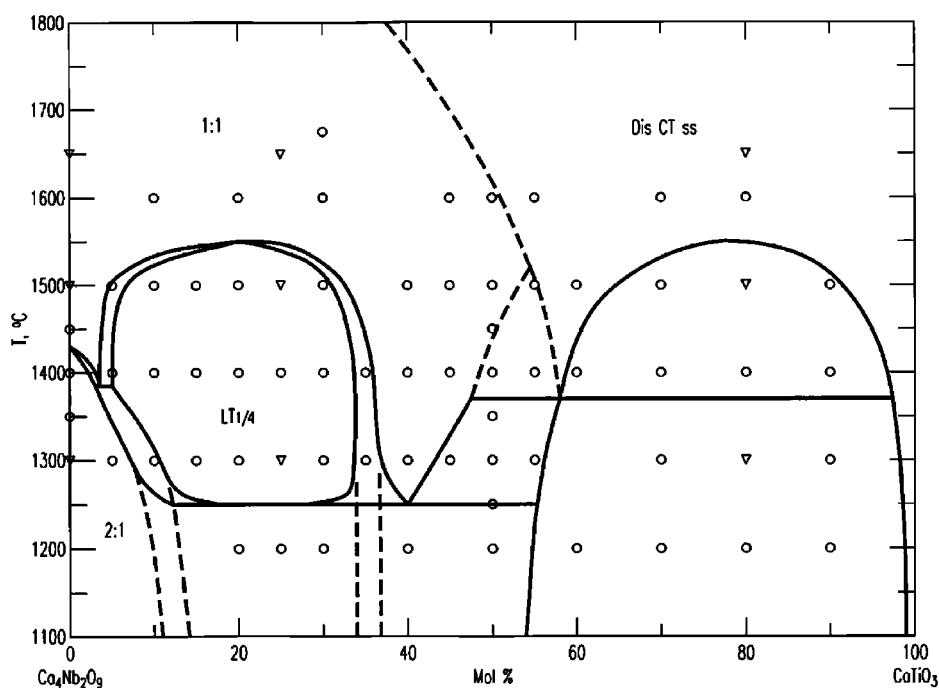| Polymorphs	Temperature of existence	Space group, #	Ordering **k** vector	Tilt/ordering
Cubic (C)	$> 1600°$C?	$Pm3m$, # 221	None	None
Cubic ordered (CO)	$> 1600°$C?	$Fm3m$, # 225	$\frac{1}{2}[111]_C^*$	None + 1:1(111)$_C$
Monoclinic HTP$_2$^{a}	1450°C–1600°C	$P2_1/c$, # 14	$\frac{1}{2}[111]_C^*$	$a^-b^+a^-$ + 1:1(111)$_C$
Monoclinic LT$_{1/6}$	$< 1450°$C	$P2_1/c$, # 14	$\frac{1}{6}[111]_C^*$	$a^-b^+a^-$ + 1:2(111)$_C$
Triclinic LT$_{1/4}$	Metastable	$P1$, # 1	$\frac{1}{4}[111]_C^*$	$a^-b^+a^-$ + 1:3(111)$_C$

^{a}Labeling of phases is according to (4).

FIG. 3. Phase equilibrium diagram of the system $Ca_4Nb_2O_9$–$CaTiO_3$ according to the interpretation of only X-ray powder diffraction data. Circles represent the compositions and temperatures at which specimens were annealed. Inverted triangles represent composition/temperature of specimens quenched to examine reversal from 1650°C equilibrium.

slurry. Mixtures were pressed into pellets and placed on beds of sacrificial powder of the same composition on Pt foil supported in alumina combustion boats. After an initial overnight calcine at 1000°C, reactions were completed by multiple heatings at 1375°C to 1425°C. The details of final heat treatments for different compositions are summarized in Tables 3–6. Finally, the specimens were sintered at tem-

peratures ranging from 1450°C to 1500°C. According to X-ray energy dispersive spectroscopy (EDS), no significant deviation from the nominal composition was detected for all specimens.

The TEM specimens of $x = 0.1$, 0.25, 0.5, and 0.8 compositions were prepared from dense pellets by conventional polishing, dimpling, and ion thinning. The specimens were

TABLE 3
List of Heat Treatments and Corresponding Microstructural Observations for $x = 0.8$ Specimens

Specimens	Heat treatments: temp. (°C)/time (h)	Observed structures and ordering	Equilibrium phase at the temperature of heat treatment
A	1600/65,	Single-phase twinned *Pnma*, no ordering	C (*Pm3m*)
B	A + 1500/300	Single-phase (O_{av}.) twinned *Pnma*, no ordering	C (*Pm3m*)
C	A + 1450/5, 50	Residual O_{av}. + high-Ti twinned *Pnma* O_2 + low-Ti HTP$_2$ (with quenched LT$_{1/4}$)	Transition to two-phase field C ($x = 0.93$) + O$'_2$($x = 0.7$)
D	A + 1450/500	High-Ti twinned *Pnma* O_2 + low-Ti HTP$_2$ (with quenched LT$_{1/4}$)	Two-phase field C ($x = 0.93$) + O$'_2$($x = 0.7$)
E	A + 1400/10, 50	Residual O_{av}. + high-Ti *Pnma* O_2 + low-Ti HTP$_2$ (with quenched LT$_{1/4}$)	Transition to two-phase field O_2 ($x = 0.93$) + O$'_2$($x = 0.66$)
F	A + 1300/24, 50, 66, 100, 200	High-Ti *Pnma* O_2 + low-Ti HTP$_2$ (with quenched LT$_{1/4}$)	Two-phase field O_2($x = 0.95$) + O$'_2$($x = 0.6$)
G	A + 1300/500	High-Ti *Pnma* O_2 + low-Ti HTP$_2$ (with quenched LT$_{1/4}$)	Two-phase field O_2($x = 0.95$) + O$'_2$($x = 0.6$)
H	A + 1050/100	Single-phase (O_{av}.) twinned *Pnma*	O_2 ($x = 0.8$)
I	A + 1000/100	Single-phase (O_{av}.) twinned *Pnma*	O_2 ($x = 0.8$)

TABLE 4
List of Sintering Temperatures, Heat Treatments, and Corresponding Microstructural Observations for $x = 0.5$ Specimens

Specimens	Sintering temperature, heat treatments: temp. (°C)/time (h)	Observed structures and ordering	Structure at the temperature of a heat treatment
A	As-sintered, 1550/3	Twinned structure $LT_{1/4}$, diffuse reflections	C ($Pm3m$)
A/B.	A + 1000 /10	$LT_{1/6}$ precipitates	$LT_{1/6}$ + O_2
A/C	A + 1100/100	Twinned structure $LT_{1/4}$, diffuse reflections	HTP_2
A/D	A + 1200/100	Twinned structure $LT_{1/4}$, diffuse reflections	HTP_2
A/E	A + 1300/100	Twinned structure $LT_{1/4}$, diffuse reflections	HTP_2
B	As-sintered, 1525/3	Twinned structure $LT_{1/4}$, diffuse reflections	C ($Pm3m$)
C	As-sintered, 1500/3	Equiaxed grains $LT_{1/4}$, diffuse reflections	HTP_2
D	As-sintered, 1475/3	Equiaxed grains $LT_{1/4}$, diffuse reflections	HTP_2
E	As-sintered, 1450/3	Equiaxed grains $LT_{1/4}$, diffuse reflections	HTP_2
E/B	E/B: 1000 /10, 50, 100	$LT_{1/6}$ precipitates	$LT_{1/6}$ + O_2
F	As-sintered, 1425/3	Equiaxed grains $LT_{1/4}$, diffuse reflections	HTP_2

examined using a Phillips 430 TEM[1] microscope operated at 200 kV. Structural imaging was performed with a JEOL 3010-UHR microscope operated at 300 kV.

X-ray powder diffraction (XRPD) was conducted using an automated diffractometer equipped with incident Soller slits, theta-compensating slits, a 0.2-mm receiving slit, a graphite monochromator, and a scintillation detector. Data were collected at ambient temperatures using $CuK\alpha$ radiation with a 0.02° 2θ step size and a 2s count time per step.

4. RESULTS

Preliminary X-ray powder diffraction study and TEM study of four compositions $x = 0.1, 0.25, 0.5,$ and 0.8, with heat treatments ranging from 1000°C to 1600°C, as well as the knowledge of phase transition temperatures of the end-members, were sufficient to establish a major outline of the $CaTiO_3$–$Ca_4Nb_2O_9$ section of the phase diagram. Addi-

[1]The use of brand or trade names does not imply endorsement of the product by NIST.

tional compositions, with a limited set of heat treatments, were used occasionally in the course of the work to verify different conclusions. In the following sections, we present TEM, XRPD, and EDS/SEM results for these four compositions.

4.1. $x = 0.8$

All $x = 0.8$ specimens were first sintered at 1600°C for 65 h, and then given subsequent heat treatments summarized in Table 3. All peaks in the XRPD pattern of specimen A (air-cooled (AC) from 1600°C) were indexable by an orthorhombic lattice with parameters close to those of $CaTiO_3$, Fig. 4. TEM observation of different [110]-type SAED patterns supports the $Pnma$ structure. The microstructure of specimen A typically consists of a complex domain structure, similar to that observed for $CaTiO_3$ (6). The domains were identified as six rotational variants (with respect to the cubic axes) of the orthorhombic phase. Very often (especially in the slow-cooled or annealed specimens) the domains form a well-organized pattern. In such micro-

TABLE 5
List of Heat Treatments and Corresponding Microstructural Observations for $x = 0.1$ Specimens[a]

Specimens	Heat treatments: temp (°C)/time (h)	Observed structures and ordering	Structure at the temperature of a heat treatment
A	1600/24, WQ	$LT_{1/4}$, diffuse reflections	C ($Pm3m$)
B	A + 1400/100, WQ	$LT_{1/4}$, diffuse reflections	HTP_2
C	A + 1400/100, AQ	$LT_{1/4}$, diffuse reflections	HTP_2
D	A + 1400/72, FC	$LT_{1/4}$, sharp reflections	HTP_2
E	A + 1300/72, AQ	$LT_{1/4}$ (diffuse) + $LT_{1/6}$	HTP_2 + $LT_{1/6}$
F	A + 1000/50, AQ	$LT_{1/6}$	$LT_{1/6}$
G	F + 1300/72, AQ	Same as E	HTP_2 + $LT_{1/6}$
H	F + 1400/100, AQ	Same as C	HTP_2

[a]FC, WC, and AQ refer to furnace cooling, water quench, and air quench, respectively.

<div align="center">

TABLE 6

List of Heat Treatments and Corresponding Microstructural Observations for $x = 0.25$ Specimens[a]

</div>

Specimens	Heat treatments: temp. (°C)/time (h)	Observed structures and ordering	Structure at the temperature of a heat treatment
A	1600/24, WQ	$LT_{1/4}$, diffuse reflections	Cubic
B	A + 1400/72, FC	$LT_{1/4}$, sharp reflections (XRPD)	HTP_2
C	A + 1400/100, WQ	$LT_{1/4}$, diffuse reflections	HTP_2
D	A + 1300/100, AQ	$LT_{1/4}$, diffuse reflections	HTP_2
E	A + 1200/100, AQ	$LT_{1/4}$ (diffuse) + $LT_{1/6}$	$HTP_2 + LT_{1/6}$
F	A + 1000/50, AQ	$LT_{1/6}$	$LT_{1/6}$

[a]FC, WC, and AQ refer to furnace cooling, water quench, and air quench, respectively.

structures, interdomain interfaces are near-planar and close to either {110}- or {100}-type planes, Fig. 5. The {110}-type interfaces separate domains (twins) having non-coinciding b-axes (between A and B regions), whereas the {100}-type interfaces separate domains (twins) with a common b-axis but switched a- and c-axes (within region B). Triple junctions of the domain consisting of both {110}- and {100}-type interfaces were frequently observed, Fig. 5. Similar microstructures were observed for the specimens of other compositions cooled from 1600°C. Occurrence of the twin-like microstructures during quenching implies the fast rate of their formation, and therefore suggests the occurrence of a displacive cubic-to-orthorhombic phase transition, and the existence of a disordered cubic $Pm\bar{3}m$ phase above 1600°C. We believe that similar to the low-temperature $CaTiO_3$ polymorph, the displacive transition occurs by the $a^-b^+a^-$ tilt of octahedra.

Annealing at temperatures ranging from 1300°C to 1450°C results in the formation of two orthorhombic phases (high and low Nb) from a compositionally metastable orthorhombic phase of a nominal composition. The phases form primarily by grain boundary precipitation, as illustrated in the back-scattered SEM image, Fig. 6a. The final morphology, Fig. 6b, suggests a diffusion-coupled reaction, similar to discontinuous precipitation or eutectoid reaction. Electron microprobe EDS showed the composition of the precipitated phases to be Ti-rich ($x = 0.93$ to 0.95) and Nb-rich ($x = 0.6$ to 0.7), respectively (Table 3). XRPD (see Fig. 3) also supports the formation of two orthorhombic, $CaTiO_3$-type phases, having slightly different lattice parameters. In Fig. 3 (specimen F, Table 3, annealed at 1300°C for 66 h) an X-ray pattern shows the peaks of the initial phase (of a nominal composition) split into triplets corresponding to (1) a smaller unit cell (close to $CaTiO_3$, marked as O_2), (2) a larger unit cell (marked as O'_2), and (3) the residual phase (marked as O_{av}). In the course of this transformation, apparently controlled by mobility of grain boundaries and grain boundary diffusion, the residual phase undergoes the following structural changes. The initial twinned structure of the air-cooled phase has poorly accommodated domains, which will result in large internal stresses. Accommodation of the stresses occurs during the annealing by rearrangement of twin interfaces, which results in the formation of alternating plate-like domains having a common
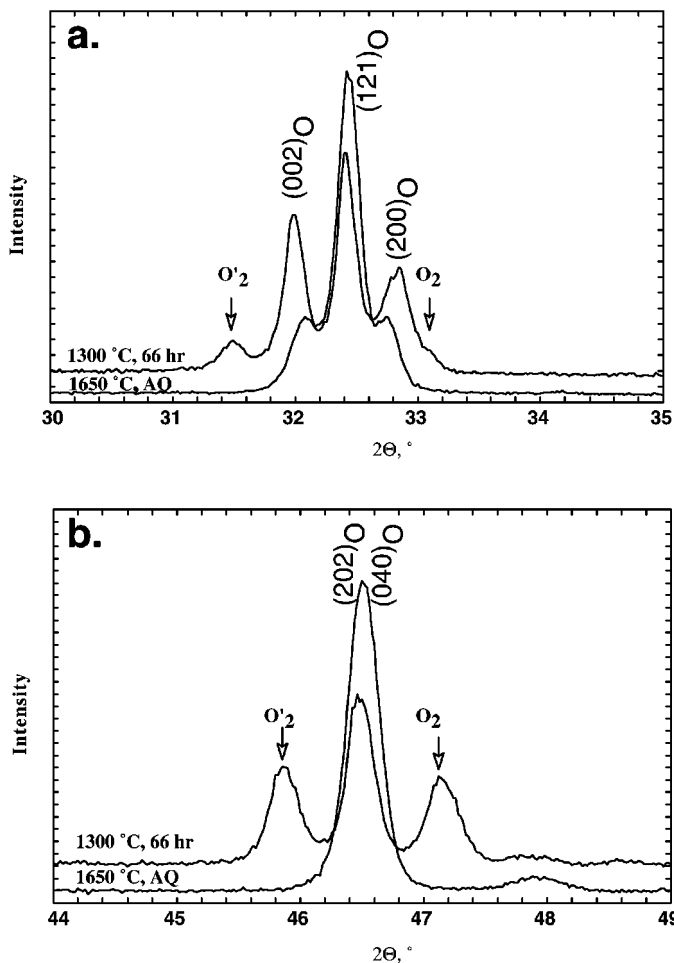

FIG. 4. (a) Portions of two XRPD patterns showing split peaks of cubic (a) (110) and (b) (200). The scans were obtained for two $x = 0.8$ specimens: lower scan for the 1600°C annealed and air-cooled A specimen, and upper scan for the F specimen annealed at 1300°C for 66 h.
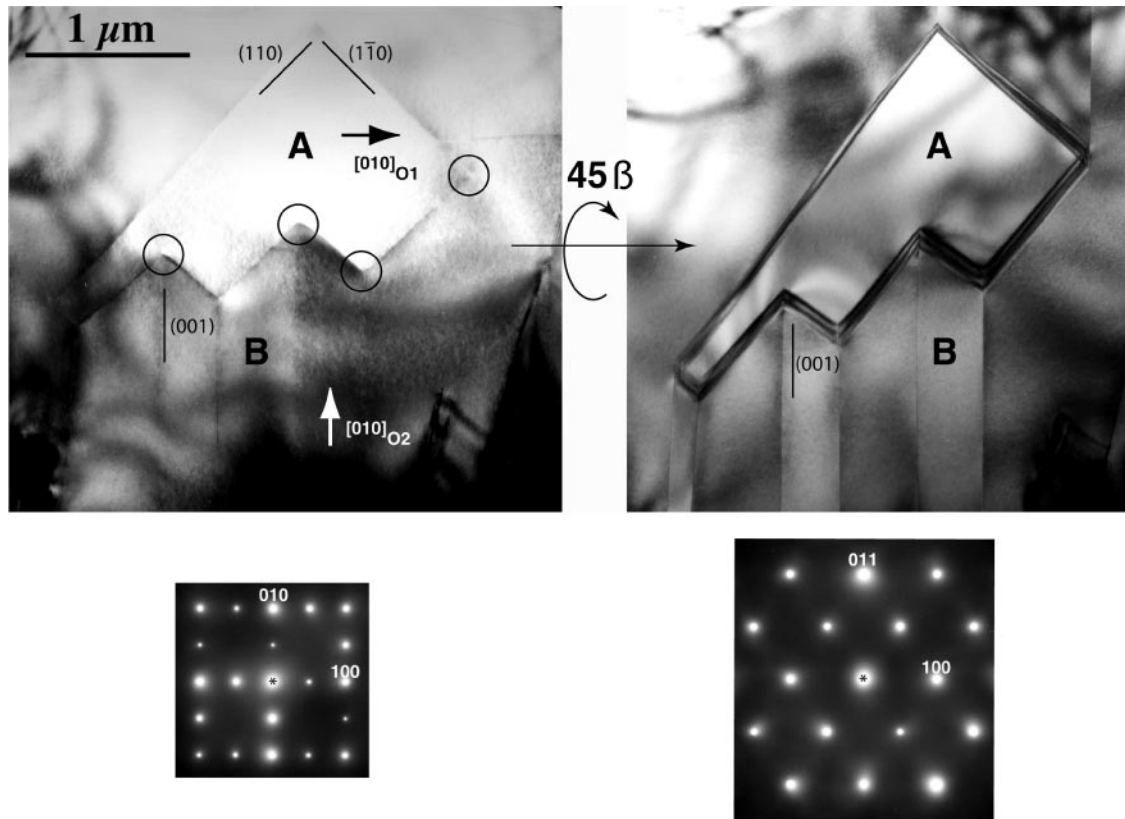
FIG. 5. Two bright field images and the corresponding SAED patterns obtained from the $x = 0.8$ I specimen (1600°C/AC and annealed at 1000°C for 100 h). Both images are of the same region but at different [001] and [011] orientations (tilted 45° around [100]*). Circles identify characteristic configurations of triple junctions in a region of impingement of orthorhombic twins with different b-axes.

b-axis and switching a/c axes (similar to that shown in Fig. 5). Homogeneous precipitation in the residual phase was detected for the specimens annealed at 1300°C. The precipitates can be readily detected after 16 h of annealing, but become more pronounced after prolonged annealing for 100 h, Fig. 7. The precipitates have a disk-like shape, with a habit plane normal to either $\langle 100 \rangle // [100]_O$ or $\langle 100 \rangle // [001]_O$. No extra reflections were detected in addition to the reflections of the orthorhombic $Pnma$.

In addition to compositional differences measured by EDS, the Ti-rich grains can be also distinguished from Nb-rich grains by the presence of a fine twinned substructure. From electron diffraction, both phases exhibit extinction of reflections corresponding to the disordered $Pnma$ structure, while the Ti-rich phase additionally features domains representing six variants of the orthorhombic lattice. From that we conclude that at 1450°C the Ti-rich phase is cubic $Pm3m$, and the domains form upon cooling. The absence of a substructure in the Nb-rich grains indicates that at 1450°C this phase has an orthorhombic $Pnma$ phase. No twinned substructure was observed in either Ti-rich or Nb-rich grains of the equilibrium two-phase mixture developed at 1300°C (after 500 h of annealing). Therefore, the

Ti-rich phase at 1300°C is in its low-temperature $Pnma$ form.

Although both precipitated phases were assumed to have $Pnma$ structure at room temperature, their diffraction patterns also differ by the presence of diffuse scattering at $\mathbf{k} = \frac{1}{4}[111]^*$ for the Nb-rich phase (Fig. 8). This diffuse scattering corresponds to the presence of domains with the LT$_{1/4}$-type ordering (see Table 2 and Fig. 2e). Similar scattering was observed for higher-Nb specimens and will be discussed in more detail in the next section. Considering the diffuse nature of $\mathbf{k} = \frac{1}{4}[111]^*$ reflections in the Nb-rich phase, we believe that the LT$_{1/4}$ ordering evolves in the course of continuous cooling from 1300°C.

4.2. $x = 0.5$

A series of specimens sintered for 2 h at temperatures ranging from 1550°C to 1425°C was investigated in their as-sintered condition by TEM (Table 4). Based on BSSEM results, all specimens appear to be a single-phase material with equiaxed grains (although slight compositional variations are also detected). TEM results on the sintered specimens are summarized in Fig. 9. According to
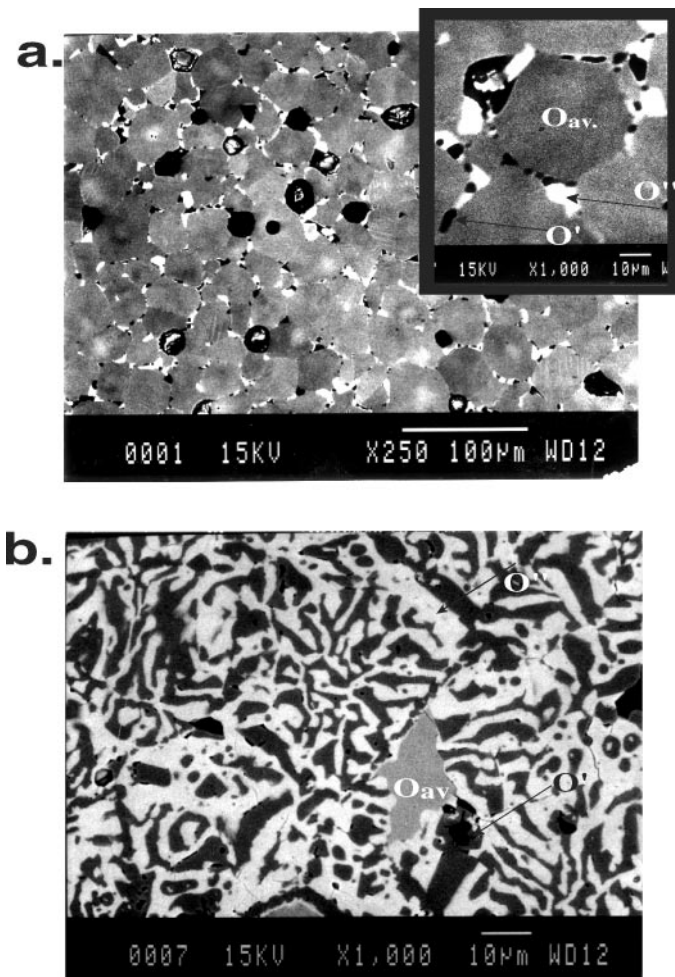
FIG. 6. Back-scattered SEM images of the $x = 0.8$ specimens C and F annealed at (a) 1450°C for 50 h and (b) 1300°C for 200 h, respectively. The composition-sensitive contrast identifies three phases, the light O_2' with high-Nb, the dark O_2 with high-Ti, and the gray residual O_{av} with a composition "in-between". The darkest round regions are pores. An inset in (a) is a magnified image of a grain with grain boundary precipitation.

microstructural observations, the specimens sintered at and above 1525°C consist of grains with a substructure of fine-scale orthorhombic twins, Fig. 9a. In contrast, no such substructure was observed in samples sintered at and below 1500°C, Fig. 9b. The observation suggests that for the $x = 0.5$ composition there is a twinning transition (similar to CaTiO$_3$ and related to the tilting of octahedra) at a temperature close to 1510°C.

SAED patterns from all $x = 0.5$ specimens exhibited the following deviations from the *Pnma* symmetry: (a) 100$_O$ and 110$_O$ sharp reflections observed for [001]$_O$ SAED patterns, Figs. 9c, 9d, and (b) diffuse scattering at $\mathbf{k} = \frac{1}{4}[111]^*$ similar to that observed for the Nb-rich phase of the two-phase $x = 0.8$ specimen (compare Fig. 8a and Fig. 9d). The presence of 100$_O$ and 110$_O$ reflections suggests 1:1 ordering, similar to that in the monoclinic (pseudo-orthorhombic)

binary Ca$_4$Nb$_2$O$_9$ $P2_1/n$ (HTP$_2$), Table 1 and Fig. 2d. In this phase the 1:1 ordering of (111) planes is combined with the $a^-b^+a^-$ tilt of octahedra. The 100$_O$ and 110$_O$ reflections can be distinguished from $\mathbf{k} = \frac{1}{4}\langle 111 \rangle^*$-type reflections by their sharpness (e.g., Fig. 9e). The 1:1 ordering reflections were observed systematically for the specimens sintered at temperatures below 1500°C. For the specimens sintered at 1550°C and 1525°C, SAED patterns with extinctions of both the disordered *Pnma* and the 1:1 ordered $P2_1/n$ were observed, Fig. 9c. This inconsistency is attributed to small compositional variations in the sintered specimens and to proximity of the sintering temperature to the 1:1 ordering transition.

Diffuse scattering at $\mathbf{k} = \frac{1}{4}\langle 111 \rangle^*$ observed in all sintered $x = 0.5$ specimens (Fig. 9c,d) was attributed to the LT$_{1/4}$-type ordering (Table 1 and Fig. 2e) which occurred on cooling from the sintering temperature. High-resolution imaging at the [001]$_O$ orientation, Fig. 10, confirmed the presence of fine domains which correspond to the two orientational variants of the LT$_{1/4}$ structure with the ordering vectors $\frac{1}{4}[111]^*$ and $\frac{1}{4}[\bar{1}11]^*$. The domains were revealed by Fourier filtering of the original HRTEM image using only $\frac{1}{4}\langle 111 \rangle$-type reflections (Fig. 10b). The image suggests ellipsoidal ordered domains, about 5 to 10 nm in size. The presence of a residual phase between these ordered domains cannot be ruled out.

To identify the temperature of the $\mathbf{k} = \frac{1}{4}\langle 111 \rangle^*$ ordering transition, the $x = 0.5$ specimens were annealed at lower temperatures (see Table 4). Annealing at temperatures between 1300°C and 1100°C did not produce any clear effect on the size of the LT$_{1/4}$ domains. However, a dramatic change in the microstructure and the ordering type occured after relatively short (10 h) annealing at 1000°C. Figure 11
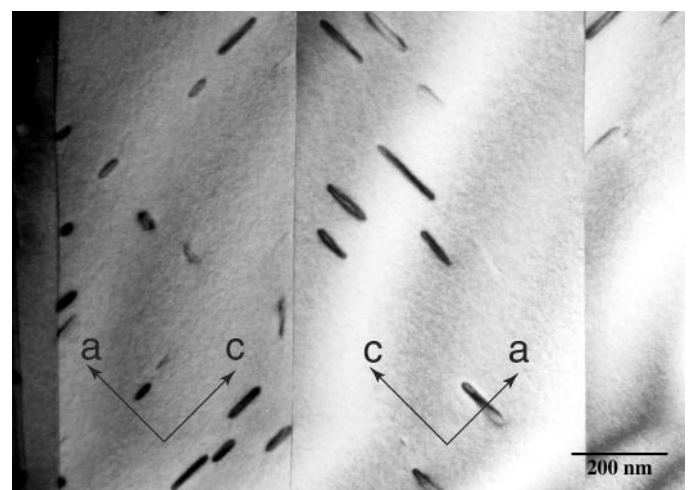

FIG. 7. Bright field image of the $x = 0.8$ specimen F annealed at 1300°C for 100 h showing disklike precipitates. Orientation of the specimen is [001]$_O$, and the habit plane of the precipitates is approximately normal to the orthorhombic *a*-axis (or *c*-axis).
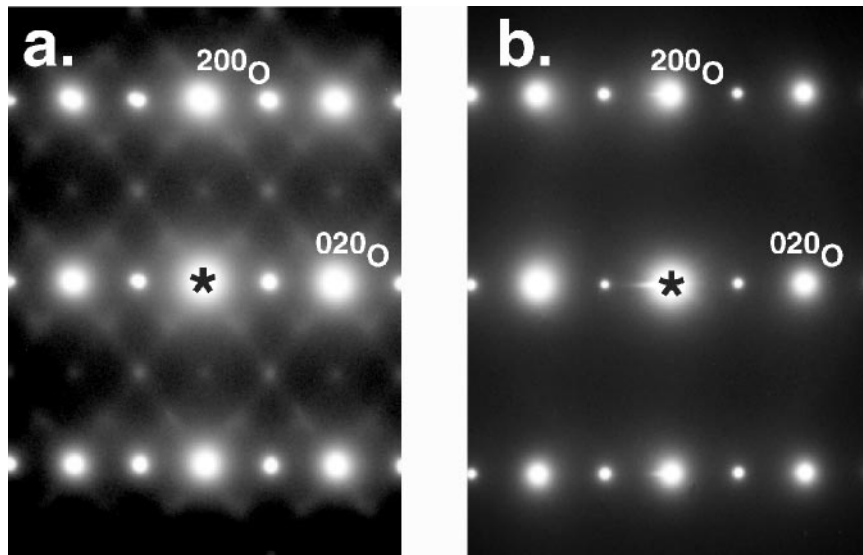
FIG. 8. SAED patterns taken from (a) a large grain of the O_2' phase and (b) a single domain of the twinned O_2 phase (the specimen G annealed at 1300°C for 500 h). The patterns are different in the presence of diffuse scattering at $\mathbf{k} = \frac{1}{4}[111]^*$ for the O_2' phase.
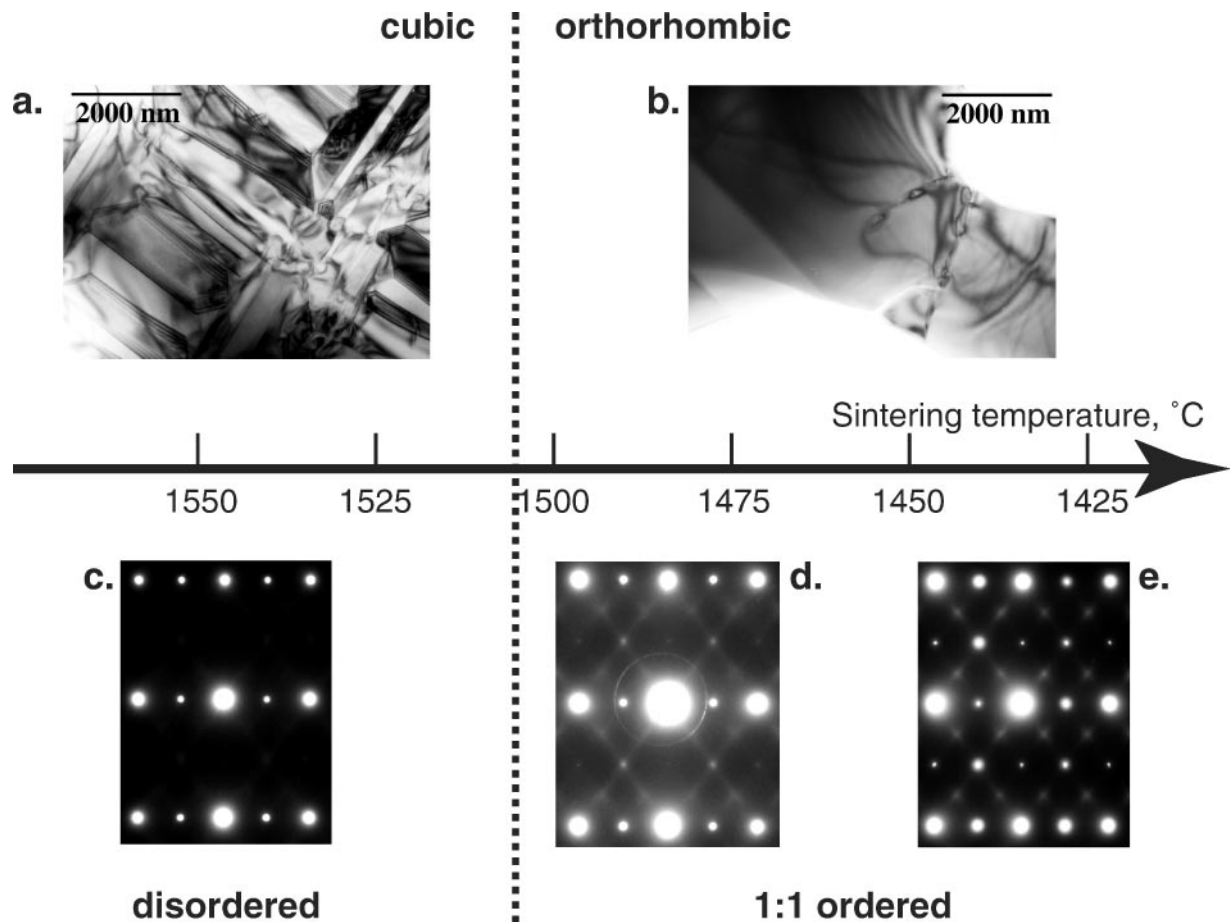

FIG. 9. Bright field TEM images (a, b) and SAED patterns (c, d, and e) of the $x = 0.5$ specimens sintered at (a, c) 1550°C, (b, d) 1500°C, and (e) 1450°C. Microstructure of the images suggests the twinning phase transition around 1500°C.
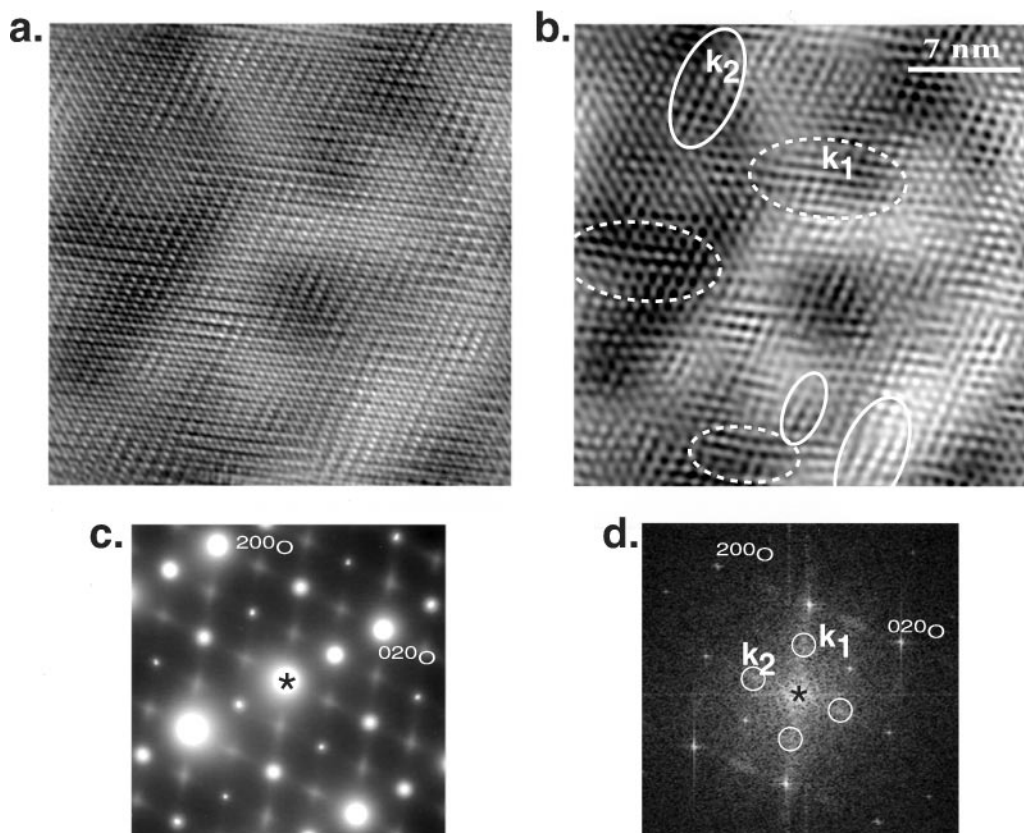
FIG. 10. Two variants of the $\frac{1}{4}[111]^*$ ordered domains observed by high-resolution imaging (the $x = 0.5$ specimen D sintered at 1475°C). (a) HRTEM image; (b) corresponding $[001]_O$ SAED pattern, (d) FFT power spectrum of the HRTEM image; and (c) reconstruction of the image using only k_1 and k_2 $\frac{1}{4}\langle 111\rangle^*$ diffuse reflections (encircled in (d)). Selected nanodomains of two 1:3 ordered variants are emphasized by encircling.

shows $[001]_O$-type SAED patterns recorded from the 1450°C-sintered specimen, Fig. 11a, which was subsequently annealed at 1000°C for different times, Figs. 11b–11d. In these SAED patterns, the $\frac{1}{4}\langle 111\rangle^*$ diffuse scattering in the as-sintered specimen (the $\frac{1}{4}$ positions are shown with circles in Figs. 11a,11b) is replaced by the $\frac{1}{3}\langle 111\rangle^*$ scattering. A locus of this scattering has an ellipsoidal shape, with elongation in $\langle 111\rangle^*$ direction. The $\frac{1}{3}\langle 111\rangle^*$ scattering sharpens after prolonged annealing, Fig. 11d. The SAED patterns containing $\frac{1}{3}\langle 111\rangle^*$-type reflections are consistent
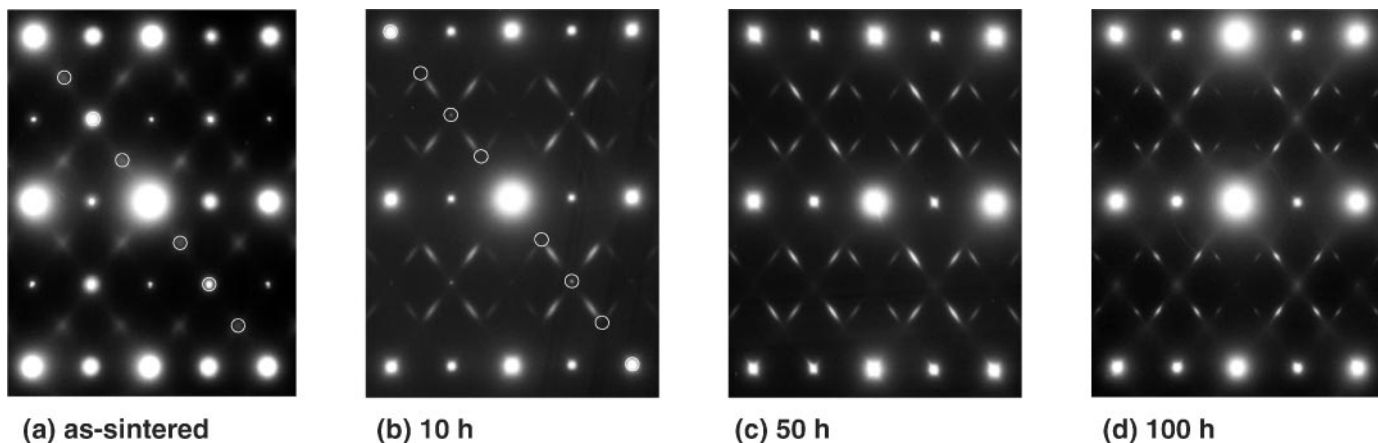

FIG. 11. A series of $[001]_O$-type SAED patterns taken from the 1450°C sintered specimens (a) which was subsequently annealed at 1000°C (E/B) for (b) 10, (c) 50, and (d) 100 h. The circles in (a) and (b) are at $\frac{1}{4}[111]^*$ locations.
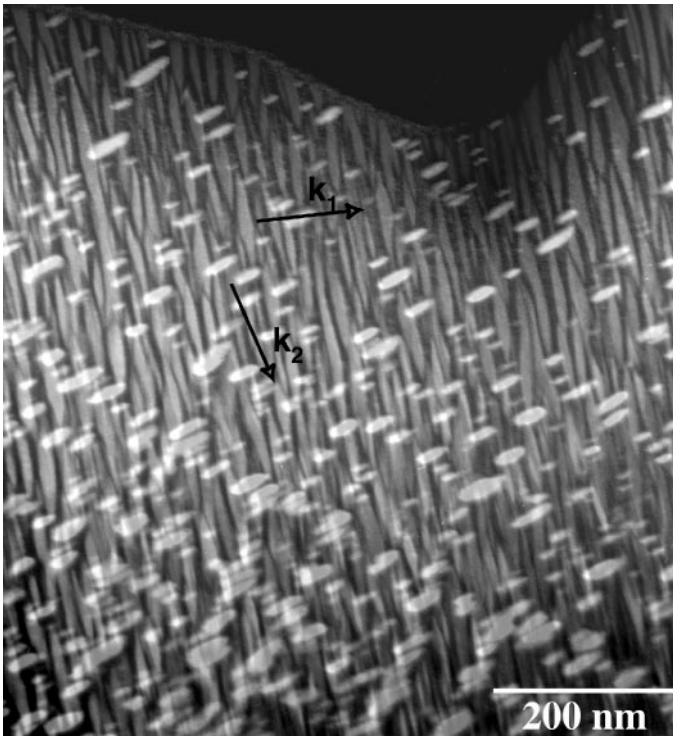
FIG. 12. Dark field image of homogenous precipitates (near the [001]$_o$ zone axis) obtained for the $x = 0.5$ specimen A/B annealed at 1000°C for 100 h. The two variants of the precipitates were imaged separately at near-two-beam conditions using the $\frac{1}{3}[111]_C^*$ and $\frac{1}{3}[-111]_C^*$ reflections. Two dark field images were aligned and overlapped using the Adobe Photoshop technique of layer transparency control.

with the 1:2-ordered structure similar to the monoclinic $P2_1/c$ (LT$_{1/6}$) polymorph of binary Ca$_4$Nb$_2$O$_9$ (see Table 1 and Fig. 2c). Dark field imaging with the $\frac{1}{3}\langle 111 \rangle_C^*$ reflections, Fig. 12, demonstrates that the 1000°C annealing results in the formation of two rotational variants of the $\frac{1}{3}\langle 111 \rangle_C^*$-ordered precipitates. In this figure two dark field images of different variants (taken with a superlattice $\frac{1}{3}\langle 111 \rangle_C^*$ reflection of each variant) are overlapped by using Adobe Photoshop® layers of different transparency. The size of the precipitates (a longer axis) changes from 10–20 nm for 10 h, to about 200 nm for 100 h. Space filling in this image clearly shows the presence of the small-volume fraction of a matrix (darkest contrast). In some TEM specimens the volume fraction of the matrix was significantly higher near grain boundaries. For such near-grain boundary regions both SAED patterns and HRTEM imaging suggest a matrix with the *Pnma* structure.

The observed $\langle 111 \rangle^*$ rel-rods of intensity are the result of a *lens-like* shape of the precipitates, with the broad habit plane of the particles approximately normal to the $\langle 111 \rangle^*$ direction. The lens-like shape is demonstrated by tilting a TEM specimen around one of the $\langle 111 \rangle_C^*$ directions, Fig. 13, where the projected shape and length of one variant

of the precipitates does not change after 35° tilt. HRTEM imaging of the precipitates showed perfect coherency of the precipitates with the matrix.

4.3. $x = 0.1$ and 0.25

The final heat treatments for the specimens with $x = 0.1$ and 0.25 are detailed in Tables 5 and 6. XRPD patterns of specimens A (water quenched from 1600°C) were indexed according to the 1:1 ordered HTP$_2$ Ca$_4$Nb$_2$O$_9$ polymorph (Fig. 14). Specimens annealed at 1400°C for $x = 0.1$ (specimen B, Table 5) and at 1400–1300°C for $x = 0.25$ (specimens C and D, Table 6) yielded the same phase. Electron diffraction revealed diffuse superlattice reflections at $\mathbf{k} = \frac{1}{4}[111]^*$, corresponding to the nano-sized domains with the LT$_{1/4}$ structure, similar to the $x = 0.5$ composition, Fig. 10. These reflections were too weak to be detected by conventional XRPD. However, the $\mathbf{k} = \frac{1}{4}[111]^*$ superlattice reflections were detected by XRPD and TEM for the specimens slowly (furnace) cooled from 1400°C (specimens D, Table 5 and B, Table 6) (Fig. 16).

Annealing of the specimens at 1300°C ($x = 0.1$, specimen E) and 1200°C ($x = 0.25$, specimen E) resulted in a two-phase mixture, with one of the phases containing nano-domains of the LT$_{1/4}$ structure and the other having well-developed twins of the LT$_{1/6}$ structure (Figs. 15a, 15b). Electron diffraction (inset in Fig. 15b) shows typical SAED patterns where both $\mathbf{k} = \frac{1}{4}[111]^*$ and $\mathbf{k} = \frac{1}{6}[111]^*$ reflections are positioned along a common reciprocal direction. The LT$_{1/4}$ nano-domains apparently evolved from the HTP$_2$ (1:1 ordered) structure during cooling, as was evidenced by the lack of domain growth on prolonged annealing. Therefore, the two phases coexisting at the annealing temperatures have HTP$_2$ and LT$_{1/6}$ structures. These two phases must have different Ti content; however, the differences in compositions were too small to be determined reliably by EDS in TEM.

Further heat treatments at 1000°C produced a single phase with the LT$_{1/6}$ structure for both $x = 0.1$ and 0.25 (specimens F). Reversibility of the phase transformations (from a single phase to a two-phase field) was confirmed for the $x = 0.1$ composition using specimen G, Table 5. A high incidence of antiphase boundaries, preferentially aligned with their normal parallel to the ordering vector, was observed in the LT$_{1/6}$ phase. The size of the antiphase domains decreased strongly with increasing the CaTiO$_3$ content from $x = 0.1$ to 0.25 after similar annealings.

5. DISCUSSION

Our experimental results have shown that the xCaTiO$_3$–$(1 - x)$Ca$_4$Nb$_2$O$_9$ section of the phase diagram essentially consists of the phases that are solid solutions of the binary end-member phases. All the phases, both high- and
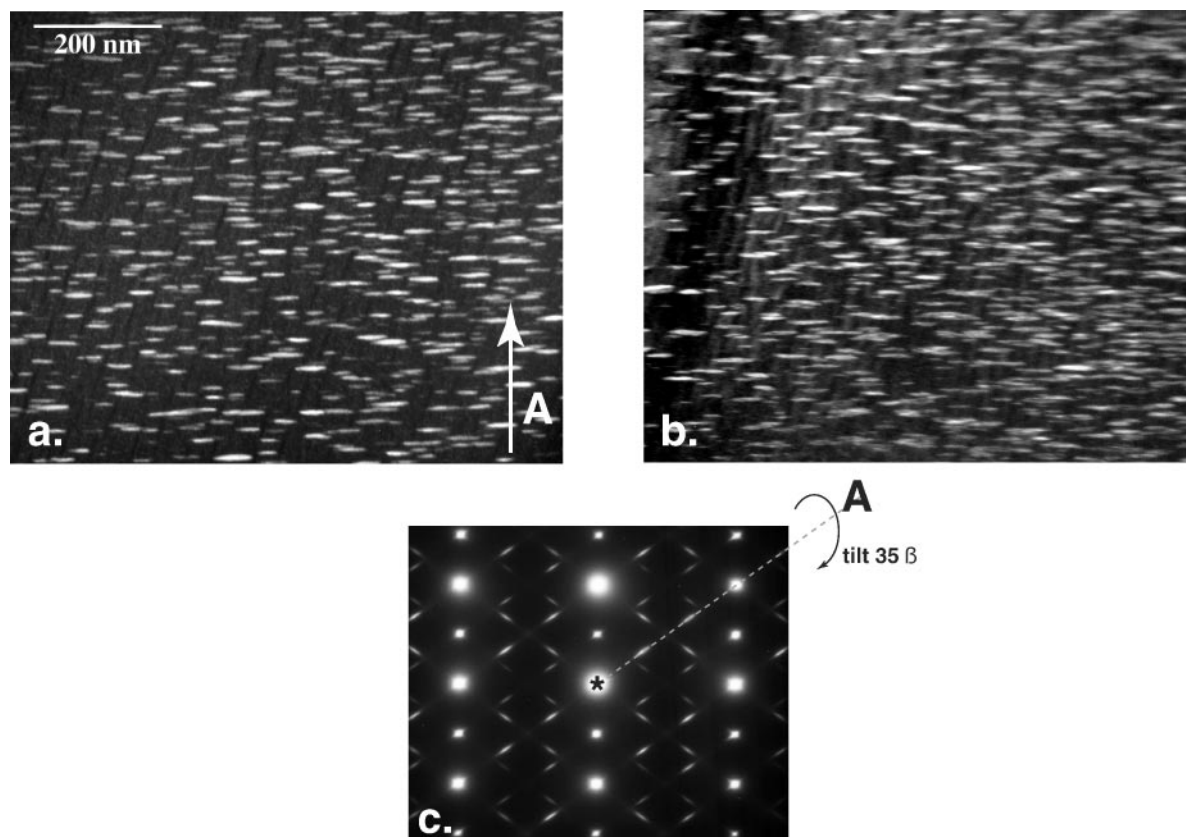
FIG. 13. Dark field images (a, b) of $LT_{1/6}$ precipitates obtained with a $\frac{1}{3}\langle 111 \rangle^*$ reflection (the $x = 0.5$ specimen E/B annealed at 1000°C for 50 h). Image (a) is near the $[001]_O$ zone axis (SAED pattern (c)) and image (b) is in the orientation after a 35° tilt around the $\langle 111 \rangle^*$ direction. The lenslike precipitates have a broad habit plane approximately normal to the $\frac{1}{3}\langle 111 \rangle^*$ direction.

low-temperature, have perovskite-like structures with a common stoichiometry $Ca[Ca_{(1-x)/(3-2x)}Nb_{(2-2x)/(3-2x)}Ti_{x/(3-2x)}]O_3$. In this formula the bracketed component is

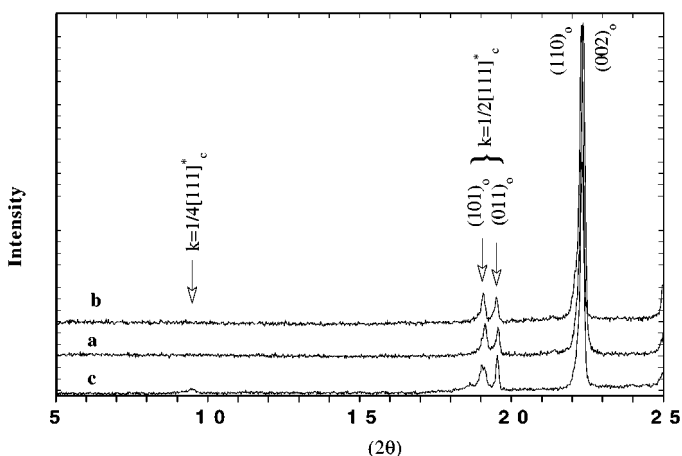**FIG. 14.** Low-2θ portions of the XRPD patterns for the $x = 0.1$ specimens with the following heat-treatments (see Table 5): (a) A, (b) C and (c) D. The peaks corresponding to the $LT_{1/4}$ phase are observed in (c), but not in (a) or (b). The reflections in the patterns (a) and (b) fit the HTP_2 phase with a combination of 1:1 ordering and $b^-b^-c^+$ octahedral tilting.

the composition of the six-coordinated B-site of the perovskite structure, and the observed different types of ordering occur only between these B-sites. Therefore, if only ordering is taken into account, the $CaTiO_3$–$Ca_4Nb_2O_9$ section represents equilibrium of structures with different types of ordering on a simple cubic lattice of B-sites. Since the ordering is either preceded or accompanied by distortions (tilting) of octahedra, only the coupling between the displacements and chemical ordering will give the true ground states and phase equilibria.

The temperature of the tilting transition decreases with increase in Ti content from about 1600°C for $Ca_4Nb_2O_9$ (4) to 1310°C (first tilting) for $CaTiO_3$ (6–9). This trend correlates with the increase of tolerance factor t from 0.82 for $Ca_4Nb_2O_9$ to 0.88 for $CaTiO_3$ [using ionic radii from (12)]; the deviation of the tolerance factor from unity represents a driving force for the tilting transition (5, 11) (instability of the ideal cubic structure). While for $CaTiO_3$ the tilting transition from a cubic $Pm3m$ to the final $Pnma$, $a^-b^+a^-$-tilted structure is spread over a large temperature range (1310° to 1110°C), for $Ca(Ca,Nb,Ti)O_3$ it appears to be a single transition combining all $a^-b^+a^-$ tilts.
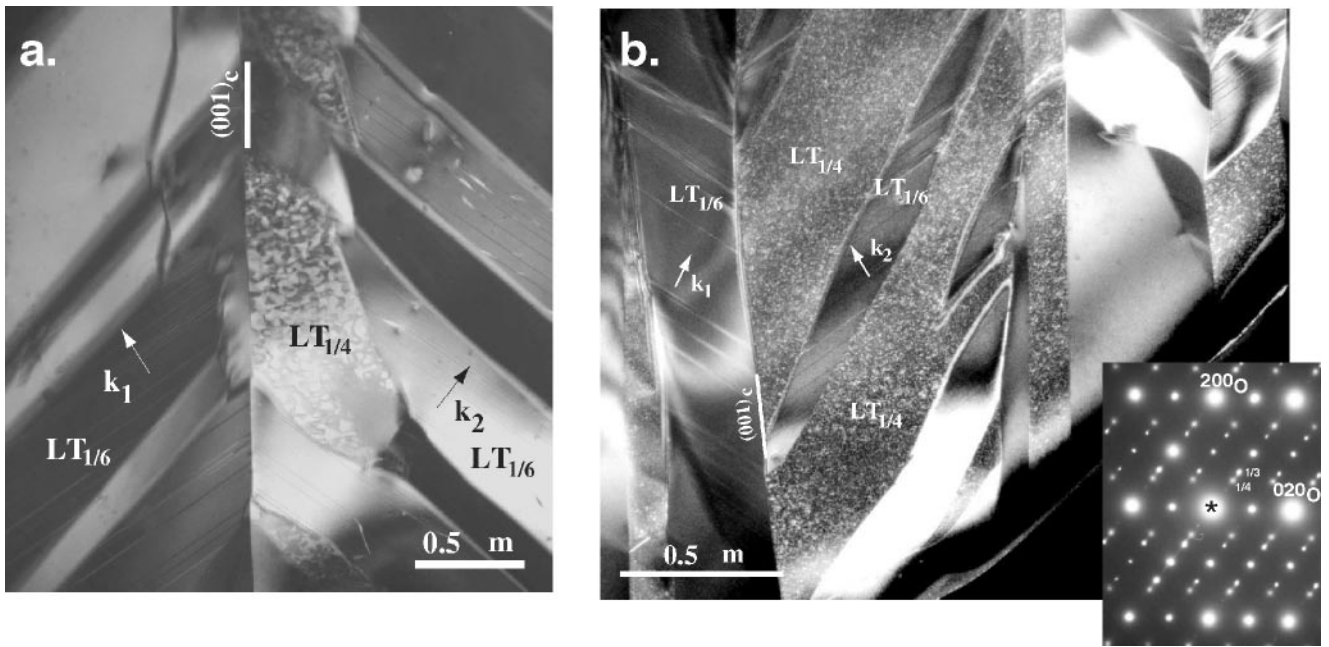
FIG. 15. Dark field image of a single grain in specimen (a) E ($x = 0.1$) and (b) E ($x = 0.25$) obtained with both $\frac{3}{4}[111]^*$ and $\frac{2}{3}[111]^*$ reflections strongly excited near the $[001]_O$ orientation (inset SAED pattern). Two phases, nano domain $LT_{1/4}$ and twinned $LT_{1/6}$, are identified in the image.

The limited number of compositions and heat treatments studied in this work has allowed us to outline only general features of the quasi-binary CaTiO₃–Ca₄Nb₂O₉ phase diagram, Fig. 16. The following two-phase fields were established: $LT_{1/6}$ ($P2_1/c$, 1:2 ordered) + O_2 ($Pnma$, disordered), $LT_{1/6}$ ($P2_1/c$, 1:2 ordered) + HTP_2 ($P2_1/c$, 1:1 ordered), and O_2 ($Pnma$, disordered) + HTP_2 ($P2_1/c$, 1:1 ordered). Only the $LT_{1/6}$ + O_2 field was established with certainty, although additional work is needed to determine precisely the phase boundaries. In other two-phase fields, the $LT_{1/6}$ + HTP_2 and O_2 + HTP_2, the presence of the HTP_2 phase was inferred by assuming that the observed $\frac{1}{4}(111)$ reflections of the $LT_{1/4}$ phase are the result of the transition from HTP_2 to metastable $LT_{1/4}$ occurring during cooling. This assumption is based on the experimental facts showing the inability of the $LT_{1/4}$ nano-domains to grow (e.g., specimens B and C for $x = 0.1$ and 0.25, respectively). Apparently, the metastable $HTP_2 \rightarrow LT_{1/4}$ transition (indicated schematically on Fig. 16 by a dashed line) is kinetically preferable (in the time scale of continuous cooling) to the stable $HTP_2 \rightarrow LT_{1/6}$ transition in a wide range of compositions ($0 < x < 0.6$). Concerning stability of the 1:3 ordered $LT_{1/4}$ phase, the stable high-temperature phase with diffraction characteristics similar to $LT_{1/4}$ was recently discovered for the 79CaO:21Nb₂O₅ composition (temperature range 1375° to 1560°C) (13). Therefore, it is plausible to assume that the $HTP_2 \rightarrow LT_{1/4}$ phase transition line is an intersection of the phase transition surface (coming from out-of-plane of CaTiO₃–Ca₄Nb₂O₉).

In studying the $x = 0.8$ composition, we found another two-phase field based on the phase separation of a disordered structure. The two-phase equilibrium in the temperature range 1450–1300°C was achieved by a sluggish eutectoid-type reaction from the metastable single O_2 phase. The low-Ti equilibrium phase was found to be disordered O_2' ($Pnma$). The high-Ti equilibrium phase is the cubic C ($Pm3m$) for 1450°C, and the O_2 ($Pnma$) for $T < 1400$°C. Considering the existence of additional CaTiO₃ polymorphs (T and O_1), we suggest a series of peritectoid reactions between 1450°C and 1400°C, as shown in Fig. 16.

According to X-ray and electron diffraction of the $x = 0.1$ and 0.25 specimens annealed at 1400°C and the $x = 0.5$ specimens sintered at < 1500°C, there is a large single-phase field of the 1:1 ordered HTP_2 phase. This phase has to be in equilibrium with the disordered O_2' phase. Since we did not establish the type of equilibrium between these phases, for simplicity we separate the phases by an ordering line, Fig. 16. The space group of the O_2 phase, $Pnma$, is of higher symmetry than the space group of the HTP_2 phase, $P2_1/c$; the space groups are in a maximal subgroup relationship (14), $Pnma \rightarrow (2) \rightarrow P2_1/n11$ ($P2_1/c$), and a second-order transition is possible.

Finally, the transition from the high-temperature cubic C ($Pm\overline{3}m$) to the HTP_2 and O_2' phases was decided to be first order, with a narrow two-phase field. Because of the displacive nature of this transition, it will be probably very difficult to establish the exact boundaries. Considering the
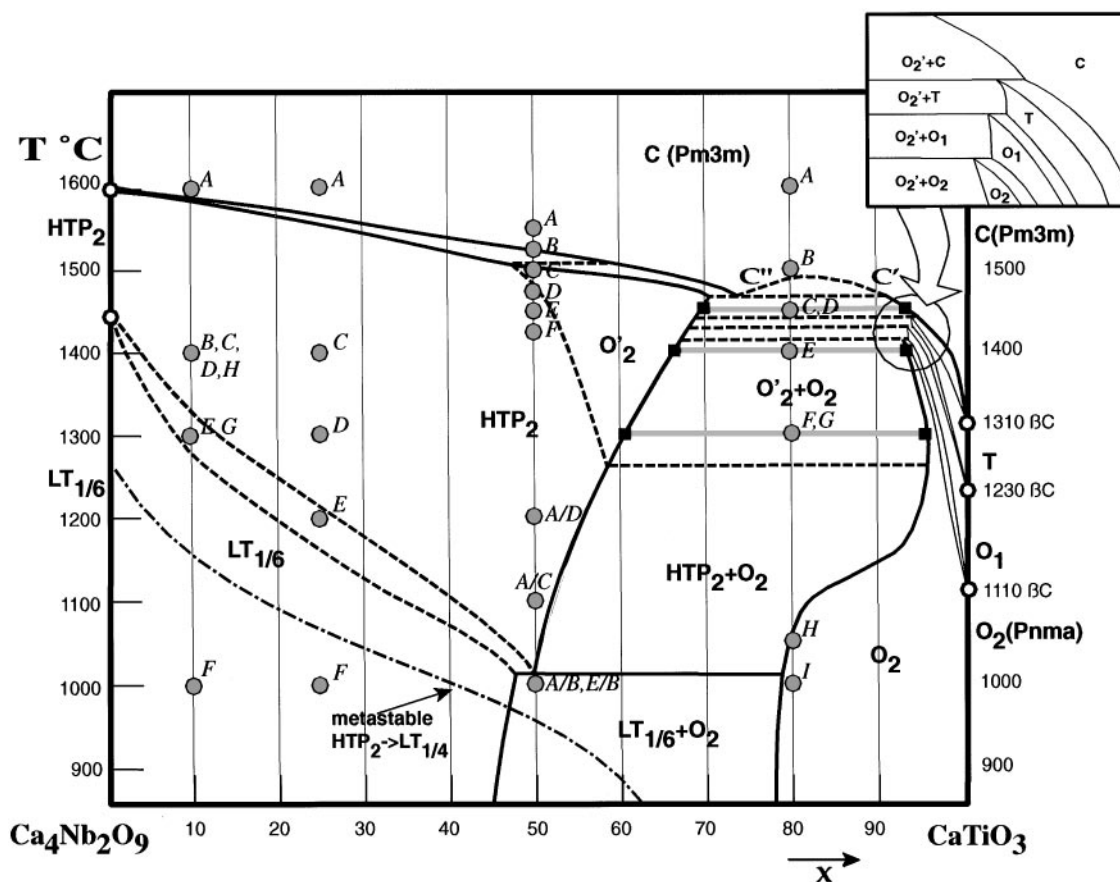
FIG. 16. A schematic drawing of the quasi-binary $CaTiO_3$–$Ca_4Nb_2O_9$ section. Circles indicate different heat treatments of $x = 0.1, 0.25, 0.5$, and 0.8 specimens (summarized in Tables 3–6). Squares show compositions of the phases in equilibrium measured by EDS for the $x = 0.8$ specimen. Inset shows blow-up of a region (encircled in the diagram) of peritectoid reactions with the $CaTiO_3$ polymorphs.

existence of a two-phase field around $x = 0.8$, we decided to connect the boundaries with the high-Ti transition $C \rightarrow T$ monotectoid reaction, with a not proven C'–C'' phase separation.

6. CONCLUSIONS

TEM was a central part of the study of the phase transformations and equilibrium of phases in the $CaTiO_3$–$Ca_4Nb_2O_9$ system because of the sensitivity of electron diffraction to chemical ordering and the ability to image microstructures. It was established that the $CaTiO_3$–$Ca_4Nb_2O_9$ system is a quasi-binary section, and all the phases participating in equilibrium are solid solutions of the binary end-members. The phases are perovskite-based ABO_3-type, with a common stoichiometry $Ca[Ca_{(1-x)/(3-2x)}Nb_{(2-2x)/(3-2x)}Ti_{x/(3-2x)}]O_3$. The differences between the lower-temperature phases is in the type of ordering between the Ca, Nb, and Ti ions occupying the B-site, as well as in the type of octahedral tilting. The proposed phase diagram

has the following single-phase fields: (1) cubic disordered C ($Pm\bar{3}m$), (2) a series of disordered $CaTiO_3$-type polymorphs T, O_1, and O_2 ($Pnma$) with different combinations of tilting; (3) low-Ti disordered/tilted O_2' ($Pnma$); (4) 1:1 ordered/tilted HTP_2 ($P2_1/c$); (5) 1:2 ordered/tilted $LT_{1/6}$ ($P2_1/c$). The single-phase fields are related to each other (Fig. 18) by the following reactions: (1) high-temperature monotectoid $C \rightarrow C' + O_2'$; (2) miscibility gap $C' + C''$; (3) eutectoid $HTP_2 \rightarrow LT_{1/6} + O_2$; (4) a series of peritectoid reactions between O_2' and $CaTiO_3$ polymorphs; (5) an ordering transition $O_2' \rightarrow HTP_2$. In addition, a metastable transition to the 1:3 ordered $LT_{1/4}$ ($P1$) phase was observed for a wide range of compositions ($0 < x < 0.6$).

REFERENCES

1. W. Wersing, *Curr. Opin. Solid State Mater. Sci.* **1,** 715 (1996); "Materials and Processing for Wireless Communications," (T. Negas and H. Ling, Eds.), Ceramic Transactions 53, Am. Ceram. Soc., Westerville, Oh., 1995.

2. R. J. Cava, J. J. Krajewski, and R. S. Roth, *Mater. Res. Bull.* **34,** 355 (1999).

3. M. Hervieu, F. Studer, and B. Raveau, *J. Solid State Chem.* **22,** 273 (1977).

4. I. Levin, L. A. Bendersky, J. P. Cline, R. S. Roth, and T. A. Vanderah, *J. Solid State Chem.* **150,** 43 (2000); I. Levin, J. Y. Chan, R. G. Geyer, J. E. Maslar, and T. A. Vanderah, *J. Solid State Chem.* **156,** 122 (2001).

5. A. M. Glazer, *Acta Crystallogr. B* **28,** 3384 (1972).

6. B. J. Kennedy, C. J. Howard, and B. C. Chakoumakos, *J. Phys.: Condens. Matter.* **11,** 1479 (1999).

7. X. Liu and R. C. Liebermann, *Phys. Chem. Miner.* **20,** 171 (1993).

8. Y. Wang and R. C. Liebermann, *Phys. Chem. Miner.* **20,** 147 (1993).

9. F. Guyot, P. Richet, Ph. Courtial, and Ph. Gillet, *Phys. Chem. Miner.* **20,** 141 (1993).

10. I. N. Flerov, M. V. Gorev, K. S. Aleksandrov, A. Tressaud, J. Grannec, and M. Couzi, *Mater. Sci. Eng.* **24,** 81 (1998).

11. K. S. Aleksandrov, "Perovskitopodobnie kristalli," Nauka, Novosibirsk, 1997 (in Russian).

12. R. D. Shannon, *Acta Crystallogr. A* **32,** 751 (1976).

13. T. A. Vanderah, W. Febo, J. Y. Chan, R. S. Roth, J. M. Loezos, L. D. Rotter, R. G. Geyer, and D. B. Minor, *J. Solid State Chem.* **155,** 78 (2000).

14. "International Tables for Crystallography" (T. Hahn, Ed.), Reidel, Dordercht, 1987.